CrossMark

Horizontally Solidified Al–3 wt%Cu–(0.5 wt%Mg) Alloys: Tailoring Thermal Parameters, Microstructure, Microhardness, and Corrosion Behavior

André Barros[1] · Clarissa Cruz[3] · Adrina P. Silva[1] · Noé Cheung[3] · Amauri Garcia[3] · Otávio Rocha[1,2] · Antonio Moreira[1]

Abstract

In the present experimental investigation, Al–3 wt%Cu and Al–3 wt%Cu–0.5 wt%Mg alloys castings are produced by a horizontal solidification technique with a view to examining the interrelationship among growth rate (G_R), cooling rate (C_R), secondary dendrite arm spacing (λ_2), Vickers microhardness (HV), and corrosion behavior in a 0.5 M NaCl solution. The intermetallic phases of the as-solidified microstructures, that is, θ-Al$_2$Cu, S–Al$_2$CuMg, and ω-Al$_7$Cu$_2$Fe, are subjected to a comprehensive characterization by using calculations provided by computational thermodynamics software, optical microscopy, and scanning electron microscopy/energy-dispersive spectroscopy. Moreover, electrochemical impedance spectroscopy and potentiodynamic polarization tests have been applied to analyze the corrosion performance of samples of both alloys castings. Hall–Petch-type equations are proposed to represent the HV dependence on λ_2. It is shown that the addition of Mg to the Al–Cu alloy has led to a considerable increase in HV; however, the Al–Cu binary alloy is shown to have lower corrosion current density (i_{corr}) as well as higher polarization resistance as compared to the corresponding results of the Al–Cu–Mg ternary alloy.

Keywords Aluminum alloys · Solidification · Dendritic microstructure · Intermetallic phases · Microhardness · Corrosion resistance

1 Introduction

Widely used in many fields, aluminum alloys have many attractive attributes when compared with steel, which make them prevalent to the manufacturing of products that demands lightweight, good mechanical properties, suitable corrosion resistance, and excellent electrical conductivity [1]. Particularly, the industrial importance of Al–Cu

and Al–Cu–Mg alloys (2xxx series) is mainly based on their high specific mechanical strength; in addition, their ductility and superior creep strength have been reported being influenced by the microstructures resulted not only from solidification processing conditions [2], but also from thermomechanical ones [3]. Some commercial alloys of this type are 2219, 2011, 2017, and 2024, which have been widely used in engineering applications, such as in aircraft fuselage structures, wing tension members, shear webs, and ribs [4, 5]. Given the strategic importance of the aforementioned alloys, efforts have been made on the development of mathematical models to preview the microstructure of these multicomponent alloys [6]. Currently, a number of technical compositions have already been standardized; however, new alloys based on the Al–Cu [7] and Al–Cu–Mg [8] systems have been considered and developed. Generally, Al–Cu–(Mg) alloys are used in four different conditions: as-cast, heat treated after casting, mechanically worked after casting, or worked and heat treated. In all the cases, significant cost savings could be

✉ Otávio Rocha
otavio.rocha@ifpa.edu.br; otvrocha@gmail.com

1 Institute of Technology, Federal University of Pará-UFPA, Belém, PA 66075-110, Brazil

2 Federal Institute of Education, Science and Technology of Pará-IFPA, Belém, PA 66093-020, Brazil

3 Department of Manufacturing and Materials Engineering, University of Campinas-UNICAMP, Campinas, SP 13083-860, Brazil

achieved through a better planning of the casting process since it directly affects the microstructure formation, hence improving the material application properties [9].

By examining the Al–Cu phase diagram, it can be seen that during solidification the Al-rich primary solid phase (α-Al), which is formed during cooling from the melt, depending on the solidification conditions, may have cellular and/or dendritic morphologies. Moreover, a number of intermetallic compounds (IMCs) may be formed in the interdendritic or intercellular regions, some of which are: Al_2Cu, $AlCu$, Al_3Cu_4, and Al_4Cu_9. Furthermore, IMCs such as Al_2CuMg, Al_6CuMg_4, $AlCuMg$, and Al_5Cu_6Mg may be observed in the as-cast microstructure when Mg is added to Al–Cu alloys [10]. Microstructures of a refined Al-rich matrix and homogeneously distributed IMCs have been recognized to provide superior hardness and tensile properties like ultimate tensile strength (UTS) and yield strength (YS). However, the presence of IMCs, which usually exhibits electrochemical characteristics that differ from that of the α-Al matrix, is well known for inducing localized forms of corrosion [11]. Moreover, Fe is a common impurity in Al alloys and is normally present in the form of Fe-rich IMCs, which are normally deleterious for the material properties as they are sources of crack and corrosion initiation and can enhance crack growth [12]. Therefore, a better understanding of the formation of IMCs during solidification and their effects on both mechanical and corrosion properties is essential for the development of methods for quality castings.

The directional solidification (DS) may be considered an interesting experimental technique permitting the effects of alloy solute content (C_0), growth rate (G_R), cooling rate (C_R), and temperature gradient (G_L) on the scale of dendritic structures (primary (λ_1), secondary (λ_2), and tertiary (λ_3) dendrite arm spacings) as well as on the formation, morphology, and size of IMCs, to be investigated. Silva et al. [13] used the DS technique to derive a Hall–Petch-type expression relating hardness of a ternary Sn–Zn–Cu solder alloy to the eutectic interphase spacing. Kakitani et al. [14] solidified directionally an Al–Ni eutectic alloy and have proposed experimental equations correlating tensile properties to the eutectic colony spacing. Yuan et al. [15] processed hypereutectic Nb–Si alloys by directional solidification and have shown that the morphology of the cross section of eutectic cells changed from a square morphology to a nearly round morphology with increasing growth rate. Jia et al. [16] used a Bridgman-type DS equipment to investigate the cellular/dendritic microstructural transition, which has been shown to occur for growth rates lower than 60 μm/s. Berkdemir and Gündüz [2] have analyzed Al–5 wt%Cu–(0.5–5) wt%Mg alloys grown in a Bridgman-type furnace at a constant G_L equal to 4.84 ± 0.13 K/mm under different G_R values varying from

16.7 to 83.3 μm/s. These authors have observed that both the dendrite tip radius and λ_2 values decrease as G_R and Mg contents ($C_{0\text{-Mg}}$) increase. Zhang and Zhao [17], combining simulations obtained by a 3-D cellular automaton (CA) method and experimental results, have shown that the evolution of λ_1 on an Al–11.6 wt%Cu–0.85 wt%Mg alloy sample, grown under steady-state conditions, has an exponential dependence on G_R. Bouchard and Kirkaldy [18] have grouped DS investigations into two categories: those involving solidification in steady-state heat flow and those in the transient regime. In the former category, G_L and G_R are independently controlled and maintained constant over time. In the latter, which characterizes the majority of industrial solidification processes, G_L and G_R are interdependent and change continuously over time.

Most studies on DS involving transient heat flow conditions have been carried out considering vertical upward solidification conditions (with melt on top of the solid), which is both thermally and solutally stable for alloys in which the rejected element at the solidification front induces a local liquid that is denser than the melt [19–23]. During horizontal growth, however, both thermal and composition gradients may occur in the melt bath resulting in quite complex movements by convection within the fluid. Convective flow during horizontal solidification is 3-D and may also have a significant impact on solidification thermal variables, solid/liquid (S/L) interface morphology, resulting structures, and segregation [24]. El-Bealy [25] and Mehrabian et al. [26] have also highlighted that horizontal solidification can readily be carried out in laboratory and it is of high practical significance being analogous to solidification occurring from the side walls of a large ingot.

Costa et al. [27] carried out vertical and horizontal solidification experiments with an Al–6 wt%Cu alloy under unsteady-state heat flow conditions. The authors have observed that a − 1/3 power law may be applied to represent λ_2 variation with C_R for both growth directions. Additionally, Dias Filho et al. [28] have shown that the λ_3 evolution of the same Al–Cu alloy during unsteady-state horizontal solidification may also be related to G_R and C_R by − 1.1 and − 0.55 power laws, respectively. In the study by Vasconcelos et al. [29], the microhardness (HV) dependence on microstructural features of a horizontally solidified Al–6 wt%Cu alloy has been evaluated using power and Hall–Petch-type experimental equation. In a recent investigation, Kaygısız and Marasli [30] analyzed samples of a eutectic Al–30 wt%Cu–6 wt%Mg alloy solidified in a Bridgman-type upward solidification furnace and have proposed experimental equations to represent the functional dependencies of lamellar eutectic spacings (λ_E) of both Al_2CuMg and Al_2Cu phases, HV profile, tensile strength (σ_T), and electrical resistivity (ρ) on G_R.

As pointed out by Zossi et al. [31] and Osório et al. [32], the corrosion resistance of Al-based alloys is of technological importance, particularly at the surface of castings. The analysis of the corrosion behavior of as-cast alloys is complex; however, the literature highlights solidification thermal and microstructural parameters as important factors to be considered. Yu et al. [33] analyzed the evolution of microstructure and corrosion behavior of an Al–Si–Cu–Mg alloy modified with different La contents and reported that the microstructure changed from coarse cells to fine cells with the increase in La from 0 to 0.9 wt% and that the highest corrosion resistance was associated with a fine cellular microstructure. Osório et al. [34] developed a comparative experimental study on the electrochemical behavior of directionally solidified samples of a Pb–1 wt%Sb alloy in both 0.5 M NaCl and 0.5 M H$_2$SO$_4$ solutions and have reported that the corrosion current density decreased with the increase in the sample cellular spacing for both examined electrolytes. Osório et al. [35] investigated the simultaneous effects of macrosegregation and scale of dendritic spacings in DS Al–Cu–Si alloys and concluded that the corrosion current density decreased with the decrease in λ_2 along the casting regions affected by macrosegregation. Soares et al. [36] analyzed the corrosion behavior of horizontally solidified samples of Al–Cu hypoeutectic alloys in a 0.2 M HCl solution. The authors have observed that areas that tend to grow faster (finer microstructures) have better corrosion resistance than those having coarser dendritic microstructures. Esquivel and Gupta [37] examined the corrosion behavior of Al–M (M: Mo, Si, Ti, Cr) alloys and reported that alloys produced by casting and containing coarse IMCs exhibited poor corrosion resistance. However, the Al–5 at% Cr alloy produced by high-energy ball milling exhibited a considerably improved corrosion resistance, which has been attributed to the corresponding nanoscale refinement of the alloy microstructure. Birbilis and Buchheit [11] have reported a detailed characterization of the electrochemical behavior of several IMCs in a NaCl solution. The observations have also included electrochemical characteristics of Al$_2$Cu, Al$_2$CuMg, and Al$_7$Cu$_2$Fe IMCs. Overall, it can be seen that corrosion properties are significantly affected by the microstructural characteristics, which may be modified by both alloy composition and thermal parameters applied during solidification.

Despite extensive studies on the characterization of Al–Cu–(Mg)-based alloys, e.g., microstructural evolutions of hypoeutectic Al–Cu alloys [38] and Al–Cu and Al–Cu–Mg eutectic alloys [39, 40] and on the electrochemical behavior of Al–Cu alloys [41], the mutual interaction of solidification processing variables, microstructure features, mechanical properties, and corrosion resistance of such alloys has not been completely investigated so far.

Therefore, the main purpose of this study is to analyze the growth of secondary dendritic arms of Al–3 wt%Cu and Al–3 wt%Cu–0.5 wt%Mg alloys as a function of both G_R and C_R values experienced during unsteady-state horizontal solidification. Microstructure–microhardness correlations considering the scale of the dendritic microstructure and different IMCs distributed within interdendritic regions, as well as the effect of the addition of 0.5 wt%Mg to an Al–3 wt%Cu alloy on corrosion properties, such as corrosion current density (i_{corr}) and polarization resistance, are also investigated.

2 Experimental

The chemical compositions of metals (commercially pure Al and Cu as well as Mg–7 wt%Al-based alloy), which have been used to prepare the investigated alloys, are reported in Table 1. The prepared alloys have also been subjected to quantitative and qualitative chemical analyses by a Q4 TASMAN-CCD-based optical emission spectrometer in order to obtain their chemical compositions, which are also given in Table 1.

The experimental setup used to achieve horizontal solidification of Al–3 wt%Cu and Al–3 wt%Cu–0.5 wt%Mg alloys ingots has been designed in such a way that heat is extracted only through a cooling system placed in the side wall of a stainless steel mold. The stainless steel mold used was 150 mm long, 60 mm wide, 60 mm high, and 3 mm thick, and the thermal contact condition at the metal/mold interface was standardized with the heat-extracting surface being polished. Further details concerning the applied casting assembly have also been described in previous studies [4, 42].

Thermo-Calc and its database TTAL7 (ThermoTech Aluminum Thermal Database v.7) have been applied for determination of Scheil–Gulliver non-equilibrium solidification path for each analyzed alloy. As a means to quantify both G_R and C_R profiles during horizontal solidification, continuous temperature measurements in the casting have been taken by using a set of eight fine type K thermocouples, accurately positioned with respect to the metal–mold interface considering the centerline corresponding to the longitudinal axis of the ingot, as presented in Fig. 1. These thermocouples have also been previously calibrated and connected by coaxial cables to a data acquisition system controlled by a computer. G_R values have been determined by the time derivative of a fitting function representing a plot of position of each thermocouple in the casting against time (t) of passage of the *liquidus* isotherm by each one. In order to calculate C_R values as a function of position along the length of the casting, the time derivatives of each cooling curve right after the passage of the

Table 1 Chemical compositions (wt%) of metals used and prepared alloys

Metals	Al	Fe	Ni	Cu	Mg	Si	Cr	Zn
Al	Balance	0.175	0.0148	0.024	0.0011	0.103	–	–
Cu	–	–	–	Balance	–	0.09	0.27	–
Mg–Al	6.981	0.001	0.001	0.115	Balance	0.246	–	0.631
Al–3 wt%Cu	Balance	0.22	–	3.14	–	0.04	0.02	–
Al–3 wt%Cu–0.5 wt%Mg	Balance	0.13	–	3.69	0.42	0.05	0.007	–
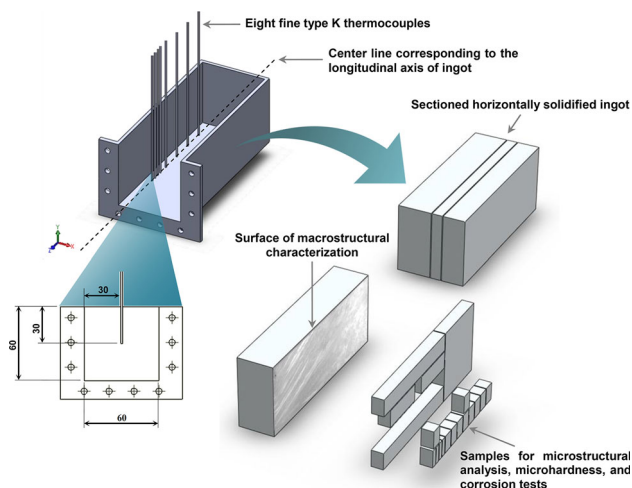
Fig. 1 Representation of both positioning of thermocouples and removal of the cast ingot samples

liquidus isotherm by each thermocouple have been computed.

A representation of removal of ingot samples is also shown in Fig. 1. After the horizontal solidification, each resulting ingot has been sectioned along its longitudinal direction (parallel to the direction of solidification). Subsequently, the metallographic specimens have been mechanically polished with abrasive papers and etched aiming to reveal the macrostructure. Etching was performed with a solution of Keller's reagent (70 ml of H_2O, 10 ml of HCl, 15 ml of HNO_3, and 5 ml of HF) during 15 s for the Al–3 wt%Cu alloy samples and with a solution of Poulton's reagent (5 ml of H_2O, 60 ml of HCl, 30 ml of HNO_3, and 5 ml of HF) during 5 s for the Al–3 wt%Cu–0.5 wt%Mg alloy samples. In order to characterize and quantify the dendritic structure, longitudinal sections of the directionally solidified samples have been extracted along the columnar zone, mechanically polished with abrasive papers, and polished and etched with a solution of 5% Keller's reagent in water during 15 s. An image processing system Olympus BX51 and the ImageJ software have been used for measurements of λ_2 by averaging the distance between adjacent side branches on longitudinal sections of primary dendritic arms [38, 43, 44], as shown in Fig. 2. At least 30 measurements were taken for each selected position along the casting length.

In addition, some samples of the alloys were subjected to microstructural characterization using a scanning electron microscope (SEM, Shimadzu, VEGA 3 SBU TESCAM) coupled to an energy-dispersive X-ray spectrometer (EDS, AZTec Energy X-Act, Oxford). Moreover, to investigate the effect of microstructure on microhardness (HV) along the length of the ingots, HV measurements were taken using a Shimadzu HMV-2 model hardness measuring test device using a 50 g load and a dwell time of 10 s. The adopted Vickers microhardness value of a representative position was the average of at least 25 different measurements on each sample. Although both λ_2 and HV values of the Al–3 wt%Cu alloy have been presented in recent studies [4, 42], the effects of 0.5 wt%Mg alloying on these features have not been investigated.

Both electrochemical impedance spectroscopy (EIS) and polarization tests have been performed on transverse samples collected at two positions along the ingot length: 10 mm (fine microstructure) and 50 mm from the cooled surface (coarse microstructure). Such electrochemical corrosion tests have been carried out in a 0.5-cm² circular area of ground and polished (1-µm diamond paste finishing) alloy samples using a stagnant and naturally aerated 0.5 M NaCl solution as the electrolyte at room temperature (25 ± 2 °C). A conventional three-electrode system, containing an Ag/AgCl reference electrode, a platinum blade as a counter electrode, and the Al–3 wt%Cu–(0.5 wt%Mg) alloys samples as the working electrodes, and an Autolab® PGSTAT128 N potentiostat/galvanostat have been used in the experiments. Electrochemical tests have been carried out in triplicate with each alloy sample aiming to verify the reproducibility.

EIS tests have been carried out using a potential amplitude adjusted at 10 mV, peak to peak (AC signal) at open-circuit potential (OCP), which has been initially measured during about 1500 s. A frequency range between 10^5 Hz to 10^{-1} Hz, 10 points per decade, was selected. In each potentiodynamic polarization test, OCP measurements have been taken during about 200 s. After this, polarization tests have been conducted by stepping the potential at a scan rate of 0.167 mV/s from − 250 to 350 mV at OCP. After this, potentiodynamic polarization curves have been plotted and both corrosion rate and potential have been estimated by Tafel plots. Figure 3
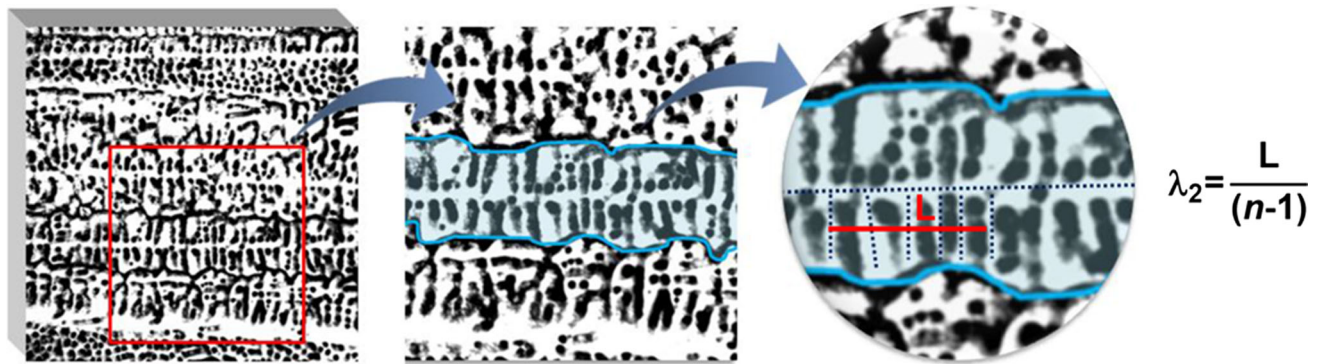
Fig. 2 Schematic representation of λ_2 measurements at longitudinal sections, in which n is the number of secondary dendritic arms
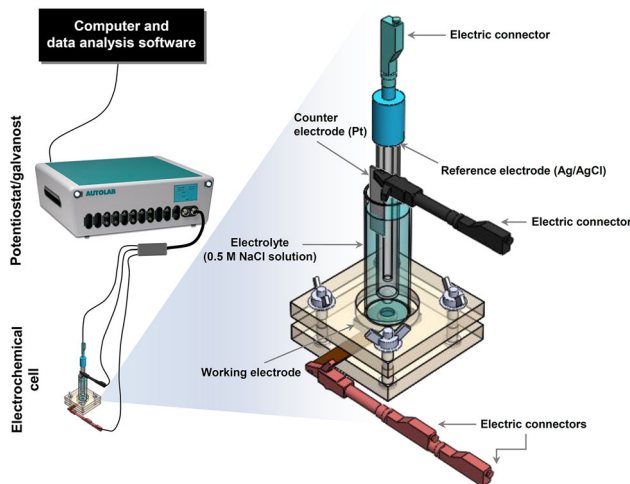

Fig. 3 Schematic diagram of the electrochemical cell applied for corrosion tests

shows the schematic design of the device used for corrosion tests.

3 Results and Discussion

Figure 4 presents the temperature–time profiles for Al–3 wt%Cu and Al–3 wt%Cu–0.5 wt%Mg alloys, where the experimental cooling curves refer to thermocouples positioned along the length of the horizontal ingot at different distances from the cooled surface considering the centerline corresponding to the longitudinal axis. Based on these thermal profiles, a plot of position from the cooled surface (P) as a function of time corresponding to the *liquidus* front passing by each thermocouple has been generated, as shown in Fig. 4c. Very similar experimental points have been found, and then, a single equation given by $P = 3.4t^{0.67}$ has been proposed for both investigated alloys ingots. The derivative of this function with respect to time has provided G_R values, as shown in Fig. 4d. In addition,

Fig. 4d also shows the experimental $C_R = f(P)$ profile that has been calculated by considering the time derivative of each cooling curve right after the passage of the *liquidus* isotherm by each thermocouple. As can be noted, higher G_R and C_R values are associated with positions near to the cooled interface because of the good surface conformity between the solidified shell and the mold surface during the initial stages of solidification. With the advance of the solidification front, decreasing profiles of both thermal variables have been observed. This can be attributed both to the thermal resistance of the solidified shell, which increases with the advance of solidification, and to the formation of air gaps at the ingot/mold interface due to thermal and volumetric contractions accompanying solidification.

The large spectra of G_R and C_R values experienced during the horizontal solidification of the Al–3 wt%Cu–(0.5 wt%Mg) alloys ingots have allowed a wide spectrum of microstructural length scales and IMCs distribution to be examined. The macrostructures and representative optical microstructures of longitudinal sections at 10, 30, and 60 mm from the metal/mold interface of the two analyzed alloys ingots are shown in Fig. 5. The macrostructure consists of elongated columnar grains inclined to the heat flow direction. This behavior of the columnar grains has provided a convincing proof that during horizontal solidification, liquid convection occurs ahead the dendritic tips, i.e., in front of the liquid/mushy interface, as reported by Murakami et al. [45]. On the other hand, there is a clear evidence that the columnar to equiaxed transition (CET) was not sharp in the investigated cases, i.e., the CET occurred in a zone rather than in a plane parallel to the chill wall, in which both columnar and equiaxed grains coexist. Similar macrostructures of horizontally solidified alloys have been reported previously [27, 46, 47].

The values of λ_2 were sufficiently distinct to make reasonably accurate measurements along the columnar region of the ingots. The average values of λ_2 as a function of distance from the cooled interface are presented in
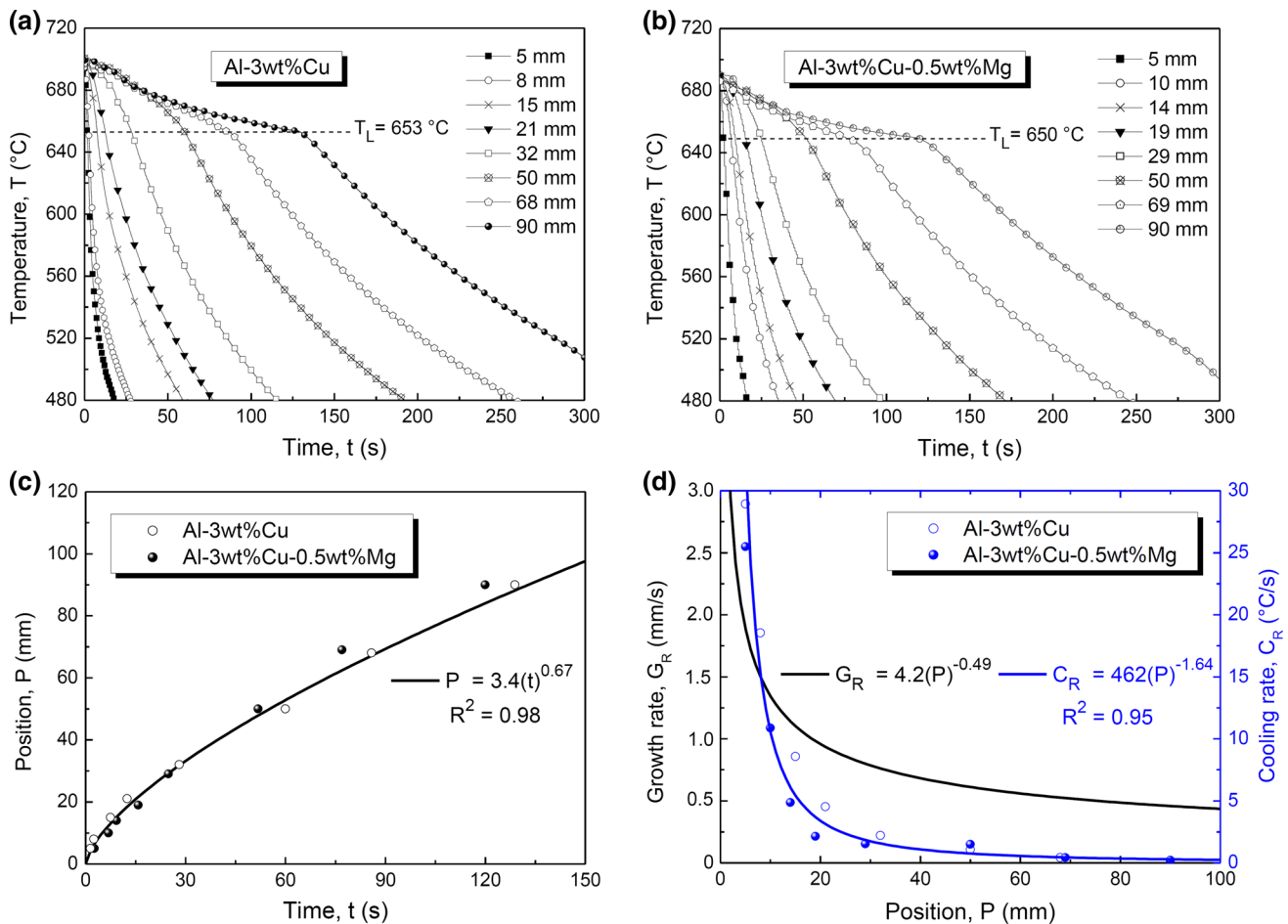
Fig. 4 Cooling curves for **a** Al–3 wt%Cu and **b** Al–3 wt%Cu–0.5 wt%Mg alloys at different positions from the cooled surface of the ingots, **c** plots of position from the cooled interface of the ingots as a function of time corresponding to the passage of the *liquidus* front by each thermocouple, **d** G_R and C_R as a function of position from the cooled interface for the two analyzed alloys ingots. R^2 is the coefficient of determination

Fig. 6, with the lines representing an experimental power function fit to the experimental points. As expected, it can be observed that λ_2 increases with the distance from the cooled interface. Figure 6 shows that, despite turbulent flows associated with melt convection during horizontal solidification, the equations given by $\lambda_2 = \text{constant} \, (G_R)^{-2/3}$ and $\lambda_2 = \text{constant} \, (C_R)^{-1/3}$ may represent the λ_2 evolution at the centerline corresponding to the longitudinal axis of the ingots. In addition, it can be noted that the addition of 0.5 wt%Mg to the binary Al–3 wt%Cu alloy has not changed these growth laws. It is worth highlighting that the $-2/3$ exponent found in the mathematical expression $\lambda_2 = f(G_R)$ is similar to that proposed by the Bouchard-Kirkaldy's model [18]. Moreover, such power growth law equations have been proposed by Rocha et al. [38] (Al–Cu alloys), Gomes et al. [48] (Al–Cu–Si alloys), and Faria et al. [49] (Al–4 wt%Cu and Al–4 wt%Cu–4 wt%Ag alloys) to describe the λ_2 growth during transient upward vertical directional solidification. Similar behavior has

been observed for other systems of nonferrous alloys directionally solidified upwards under transient conditions [50–52]. Brito et al. [53] (Al–3 wt%Mg alloy) and Spinelli et al. [54] (hypoeutectic Al–Cu alloys, including the Al–3 wt%Cu alloy) have also proposed a $-2/3$ power law to represent the λ_2 variation with G_R for downward directionally solidified samples. Likewise, Costa et al. [27] and Carvalho et al. [55] have found exponential equations of the form $\lambda_2 = \text{constant} \, (C_R)^{-1/3}$ to correlate λ_2 with C_R for horizontally solidified Al–6 wt%Cu and Al–9 wt%Si alloys, respectively.

It is well known that low Fe concentration may be present in alloys prepared from commercially pure Aluminum. However, Fe-rich intermetallic phases may be formed even for low Fe fractions. According to the Scheil–Gulliver non-equilibrium solidification path calculated by the Thermo-Calc software for the Al–3 wt%Cu and Al–3 wt%Cu–0.5 wt%Mg alloys in Fig. 7 (with 0.15 wt%Fe), the presence of Fe results in the occurrence of several Fe
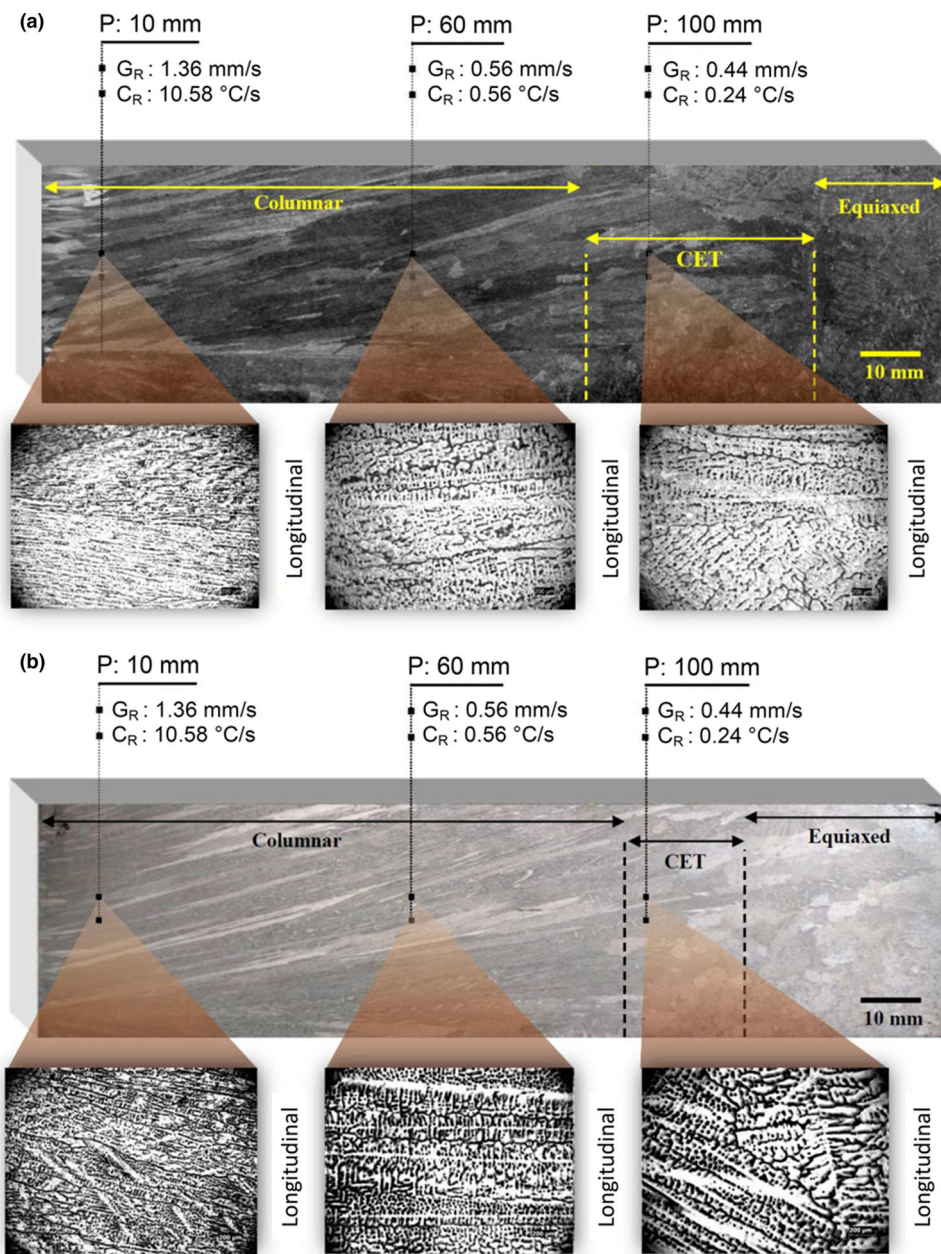
Fig. 5 Horizontally solidified macrostructure and as-cast dendritic microstructures of longitudinal sections of: **a** Al–3 wt%Cu, **b** Al–3 wt%Cu–0.5 wt%Mg alloys ingots

precipitates along liquid/solid transformation. During solidification of Al–Cu–(Mg) alloys, solute elements can also be segregated to the liquid at the solidification front and, because of different variant and invariant reactions, a number of secondary phases may form from the solute-enriched liquid. Furthermore, it is possible to note that at the end of the solidification process, the resulting microstructure will consist mainly of the Al-rich (α) primary phase and an interdendritic mixture containing the eutectic α phase and IMCs such as θ-Al_2Cu and ω-

Al_7Cu_2Fe in Al–3 wt%Cu–0.15 wt%Fe alloy, as well as S–Al_2CuMg in the ternary alloy.

A eutectic mixture formed in the Al–3 wt%Cu alloy ingot is shown in Fig. 8. Under equilibrium conditions, the occurrence of the eutectic reaction at 548 °C ($L \rightarrow (Al) + Al_2Cu$) is not expected for such alloy composition. However, when solidification occurs under non-equilibrium conditions, as in the present study, the non-equilibrium Al_2Cu phase can be formed, as observed in the interdendritic regions. Consequently, an excess of Cu in the last solid formed has occurred, which is often sufficient to
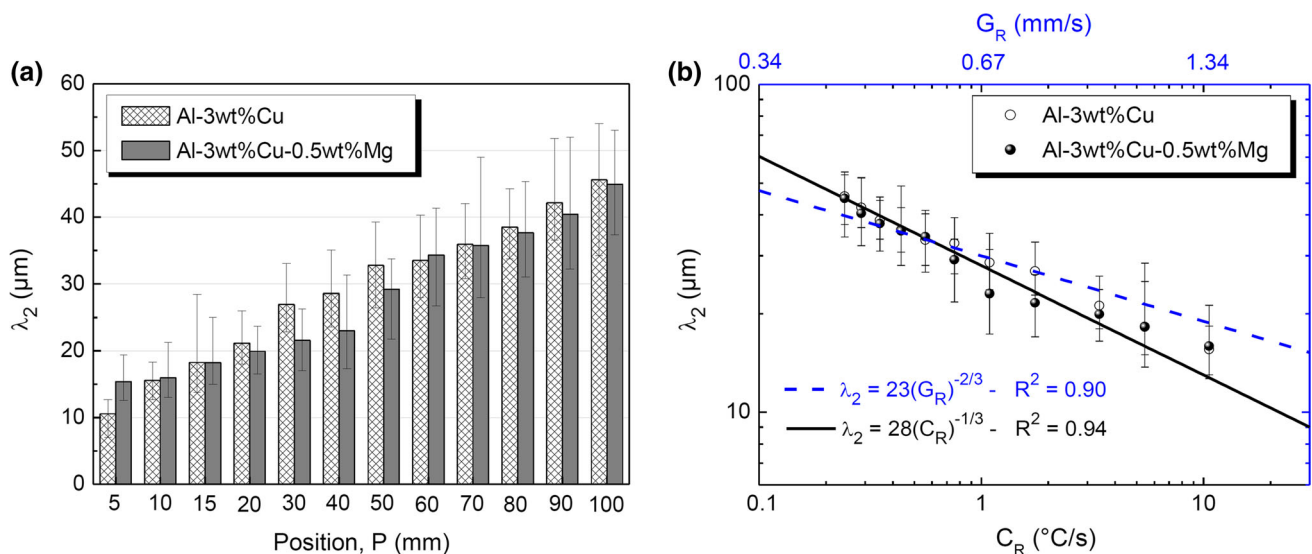
Fig. 6 Variation of λ_2 with: **a** P, **b** G_R and C_R values for both Al–3 wt%Cu and Al–3 wt%Cu–0.5 wt%Mg alloys
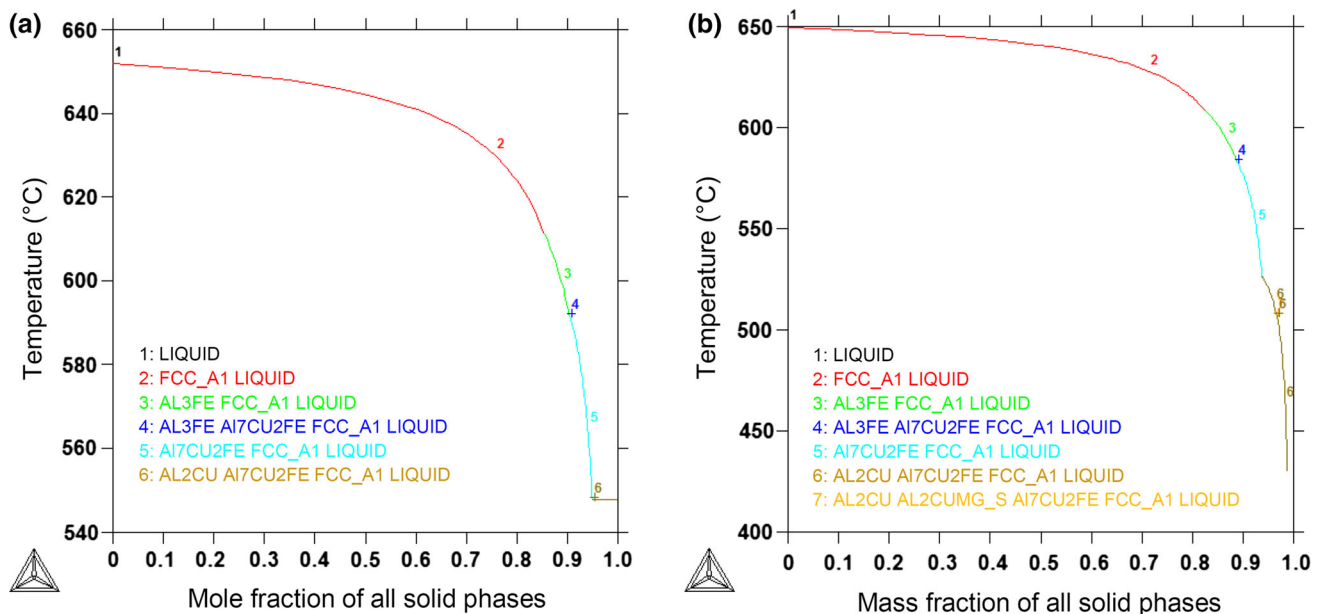

Fig. 7 Scheil–Gulliver non-equilibrium solidification path calculated by the Thermo-Calc software for **a** Al–3 wt%Cu, **b** Al–3 wt%Cu–0.5 wt%Mg alloys with 0.15 wt%Fe

result in formation of non-equilibrium eutectic Al$_2$Cu phase. The presence of both Al$_2$Cu and Fe-rich intermetallic particles has also been confirmed by the solidification path, which has indicated the presence of the eutectic mixture for the binary analyzed alloy. Moreover, Fig. 8 shows typical white-colored IMCs that can be observed for positions farther from the cooled interface of the horizontally solidified ingots.

A complete dendritic arrangement can also be observed for the ternary alloy in Fig. 8, which shows representative SEM micrographs. The identified secondary phases within

the interdendritic regions include the following IMCs: θ, ω, and S particles. Dark areas are formed by the Al-rich phase of dendritic morphology and the bright areas represent interdendritic regions that contain IMCs as indicated by the concentrations of the elements determined by EDS. Xie et al. [56] have reported a very similar microstructure for a directionally solidified Al–3.9 wt%Cu–0.9 wt%Mg alloy. Element mapping of S particles is also presented in Fig. 8. As can be seen, the addition of 0.5 wt%Mg to the Al–3 wt%Cu alloy has not modified the growth laws λ_2 versus
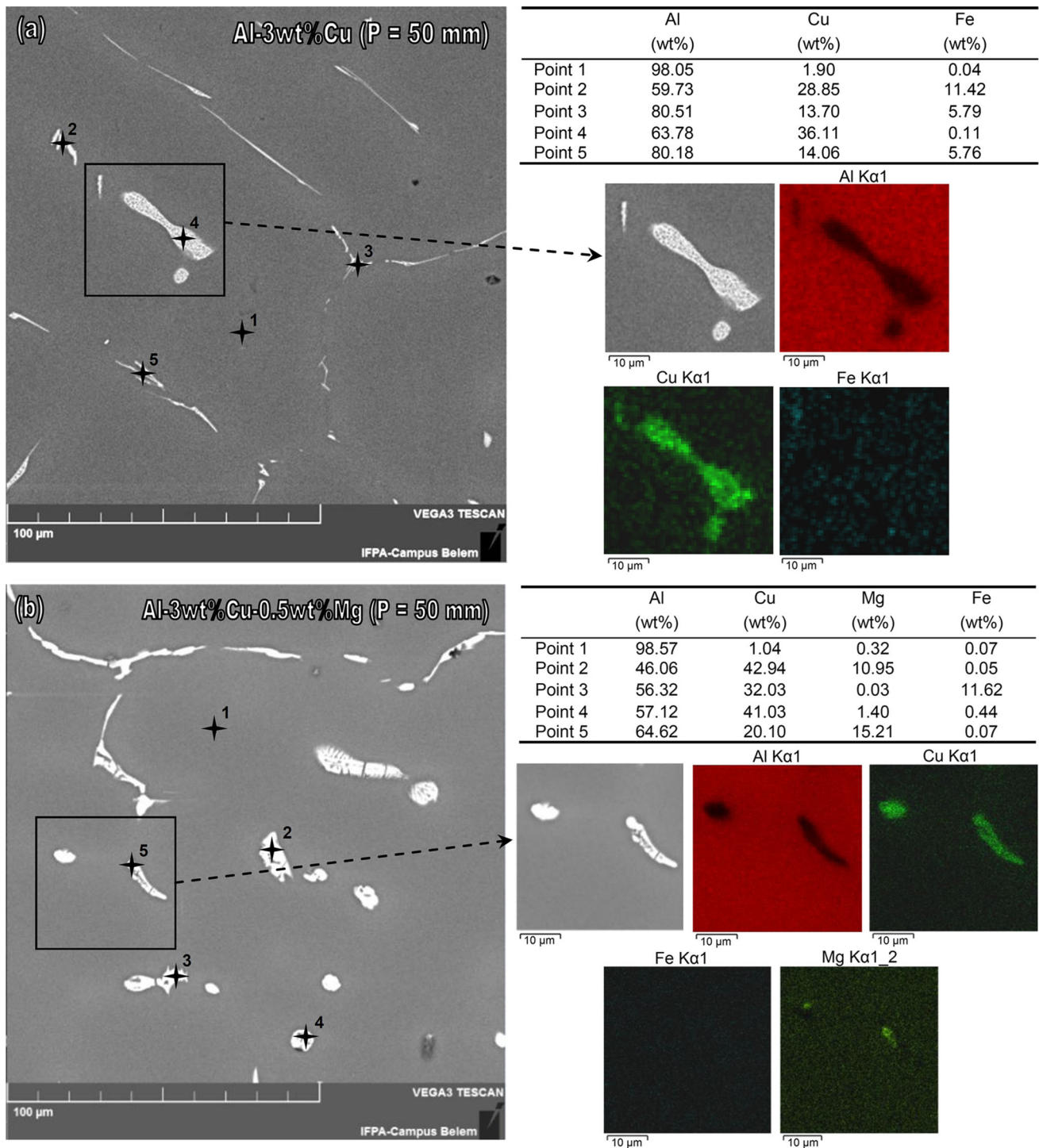
	Al (wt%)	Cu (wt%)	Fe (wt%)
Point 1	98.05	1.90	0.04
Point 2	59.73	28.85	11.42
Point 3	80.51	13.70	5.79
Point 4	63.78	36.11	0.11
Point 5	80.18	14.06	5.76

	Al (wt%)	Cu (wt%)	Mg (wt%)	Fe (wt%)
Point 1	98.57	1.04	0.32	0.07
Point 2	46.06	42.94	10.95	0.05
Point 3	56.32	32.03	0.03	11.62
Point 4	57.12	41.03	1.40	0.44
Point 5	64.62	20.10	15.21	0.07

Fig. 8 EDS element mapping and point microanalysis detailing the phases formed during the solidification process of: **a** Al–3 wt%Cu, **b** Al–3 wt%Cu–0.5 wt%Mg alloys

G_R and λ_2 versus C_R; however, a more complex arrangement of phases has been found.

Figure 9 shows the evolution of Vickers microhardness with the position from the cooled surface (P), G_R, C_R, and λ_2 for the two examined alloys. Comparing the obtained HV results of Al–3 wt%Cu and Al–3 wt%Cu–0.5 wt%Mg

alloys, it can be noted that the addition of Mg to the Al–3 wt%Cu alloy has contributed to a considerable increase in HV. One reason for this is the more complex arrangement of phases of the Al–Cu–Mg ternary alloy (α-Al + θ-Al$_2$Cu + S–Al$_2$CuMg + Fe-rich intermetallic particles) as compared to that in the Al–Cu binary alloy, as well as the
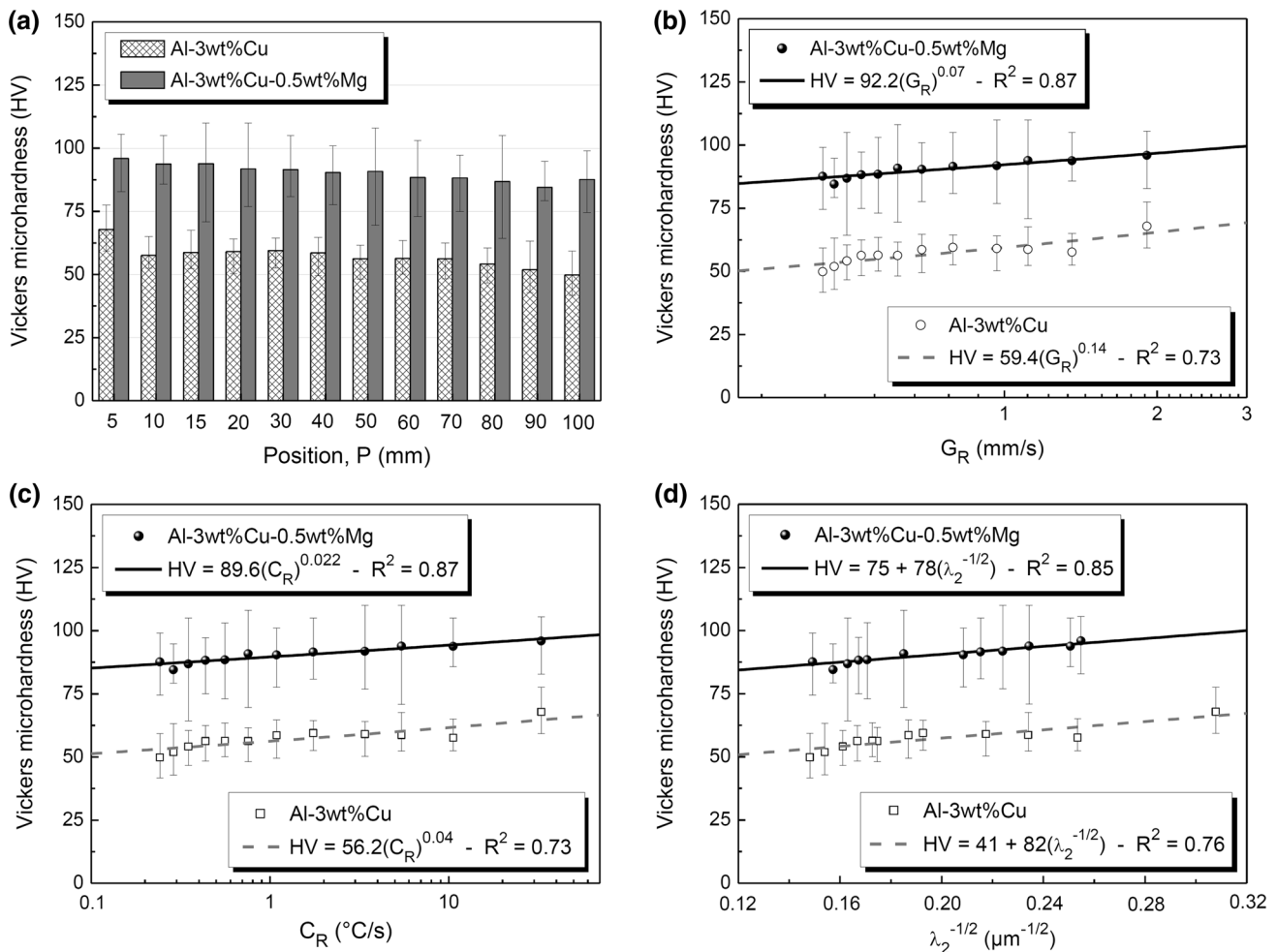
Fig. 9 Evolution of HV as a function of: **a** P, **b** G_R, **c** C_R, **d** λ_2 for Al–3 wt%Cu and Al–3 wt%Cu–0.5 wt%Mg alloys. R^2 is the coefficient of determination

distribution of Mg within the primary α-Al phase. In addition, it is well known that the mechanical strength of Al-based alloys is sensitive to changes in λ_2. Thus, for both analyzed alloys, higher HV values are associated with smaller λ_2 values, which are the typical regions of the horizontally solidified samples subjected to higher solidification rates (higher G_R and C_R values). Therefore, HV dependence on λ_2 has been characterized by Hall–Petch-type equation given by HV = $41 + 82\lambda_2^{-1/2}$ and HV = $78 + 75\lambda_2^{-1/2}$ for Al–3 wt%Cu and Al–3 wt%Cu–0.5 wt%Mg alloys, respectively.

The experimental results of EIS tests for Al–3 wt%Cu and Al–3 wt%Cu–0.5 wt%Mg alloys samples extracted from two positions: $P = 10$ mm and 50 mm from the metal/mold interface, in a naturally and stagnant 0.5 M NaCl solution at room temperature (25 ± 2 °C), are shown in Fig. 10. It is worth noting that triplicate experiments have been carried out for each alloy sample. The EIS plots in Fig. 10 represent the average values. The interpretation of Bode and Bode-phase plots (Fig. 10a) has been

performed considering three distinct ranges of frequency, i.e., low frequencies from 10^{-1} to 10^0 Hz, intermediate frequencies between 10^0 to 10^4 Hz, and high frequencies from 10^4 to 10^5 Hz. At low frequencies, the impedance modulus ($|Z|$) represents the polarization resistances of the alloy samples. Consequently, the Al–3 wt%Cu alloy sample from $P = 50$ mm has the highest polarization resistance (R_{pol}). On the other hand, the lowest polarization resistance has been verified for the ternary Al–3wt %Cu–0.5 wt%Mg alloy sample from $P = 10$ mm. The polarization resistance is directly proportional to the corrosion resistance, i.e., the higher the polarization resistance, the higher the corrosion resistance. At intermediate frequencies, double-layer characteristics and maximum phase angles (θ_{max}) have been characterized. The binary alloy samples have presented higher θ_{max} values than those of the ternary alloy samples. The solution (electrolyte) resistance has been characterized at high frequencies.

It can be seen in the experimental Nyquist plots (Fig. 10b), mainly for $P = 10$ mm samples (fine dendritic
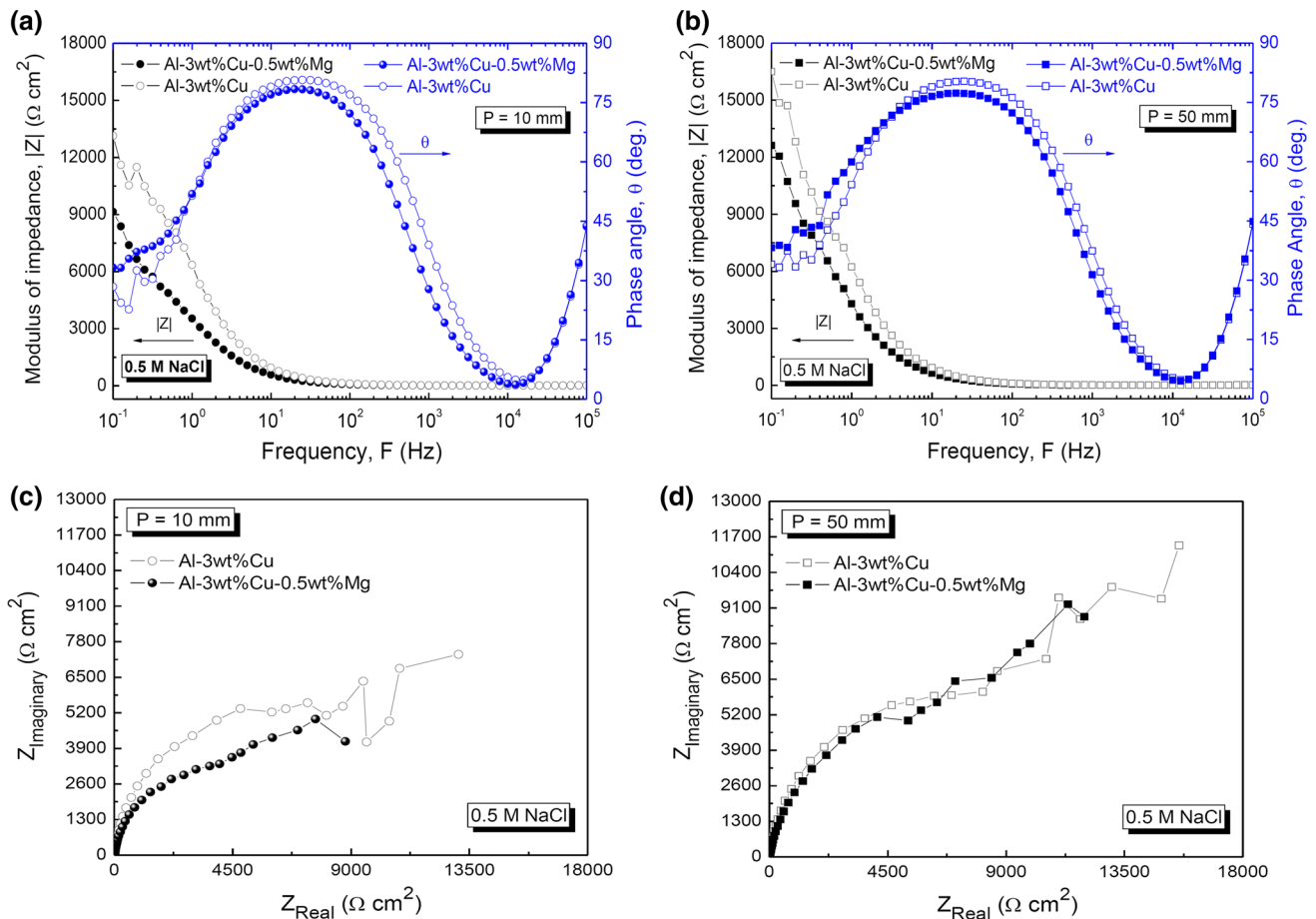
Fig. 10 Bode and Bode-phase diagrams for: **a** Al–3 wt%Cu and **b** Al–3 wt%Cu–0.5 wt%Mg alloys. Nyquist plots for: **c** Al–3 wt%Cu, **d** Al–3 wt%Cu–0.5 wt%Mg alloys samples in a 0.5 M NaCl solution at 25 °C

microstructure), the decrease in the capacitive semi-arc as a result of the addition of 0.5 wt%Mg to the Al–Cu binary alloy. It is worth noting that higher capacitive arc indicates better corrosion resistance as compared to lower ones. According to Szklarska-Smialowska [57], the formation of a passive film is one of the main reactions that occur on the surface of the sample during the initial period in which Al and Al-based alloys are immersed in aqueous solutions. The passive film on the surface can provide the protection against Cl⁻ penetration, as reported by Song et al. [58]. Therefore, better resistance and stability of the passive film (improved corrosion resistance tendency) have been found for the Al–3 wt%Cu alloy as compared to that of the Al–3 wt%Cu–0.5 wt%Mg alloy.

Since EIS parameters have indicated that the Al–3 wt%Cu alloy has a better electrochemical behavior than that of the Al–3 wt%Cu–0.5 wt%Mg alloy, potentiodynamic polarization curves have also been analyzed. Thus, Fig. 11 depicts such experimental curves obtained in a stagnant and naturally aerated 0.5 M NaCl solution at room temperature for the alloys samples at the two examined positions ($P = 10$ mm and 50 mm from metal/mold

interface). With a view to obtaining the corrosion current density (i_{corr}) using Tafel's extrapolation, both the cathodic and anodic branches of the polarization curves have been used. A lowest i_{corr} (0.103 µA/cm²) associated with a corrosion potential (E_{corr}) of − 697 mV has been attained for the sample $P = 50$ mm of the Al–3 wt%Cu alloy. On the other hand, the highest i_{corr} (1.590 µA/cm²) associated with E_{corr} equal to − 622 mV has been found for the sample $P = 10$ mm of the ternary alloy. In a general analysis, a rapid increase in the anodic current density may be seen in the polarization curves of the ternary alloy samples. Furthermore, the i_{corr} behavior of both $P = 10$ mm (fine microstructure) and $P = 50$ mm (coarse microstructure) samples has indicated that, in both cases, the addition of 0.5 wt%Mg to the binary Al–3 wt%Cu alloy has resulted in lower corrosion resistance tendency for both $P = 10$ mm and $P = 50$ mm. These observations confirm the previous trend shown by the EIS parameters, as given in Table 2. For both analyzed alloys, the differences between i_{corr} values obtained for samples at $P = 10$ mm and $P = 50$ mm have not been significant.
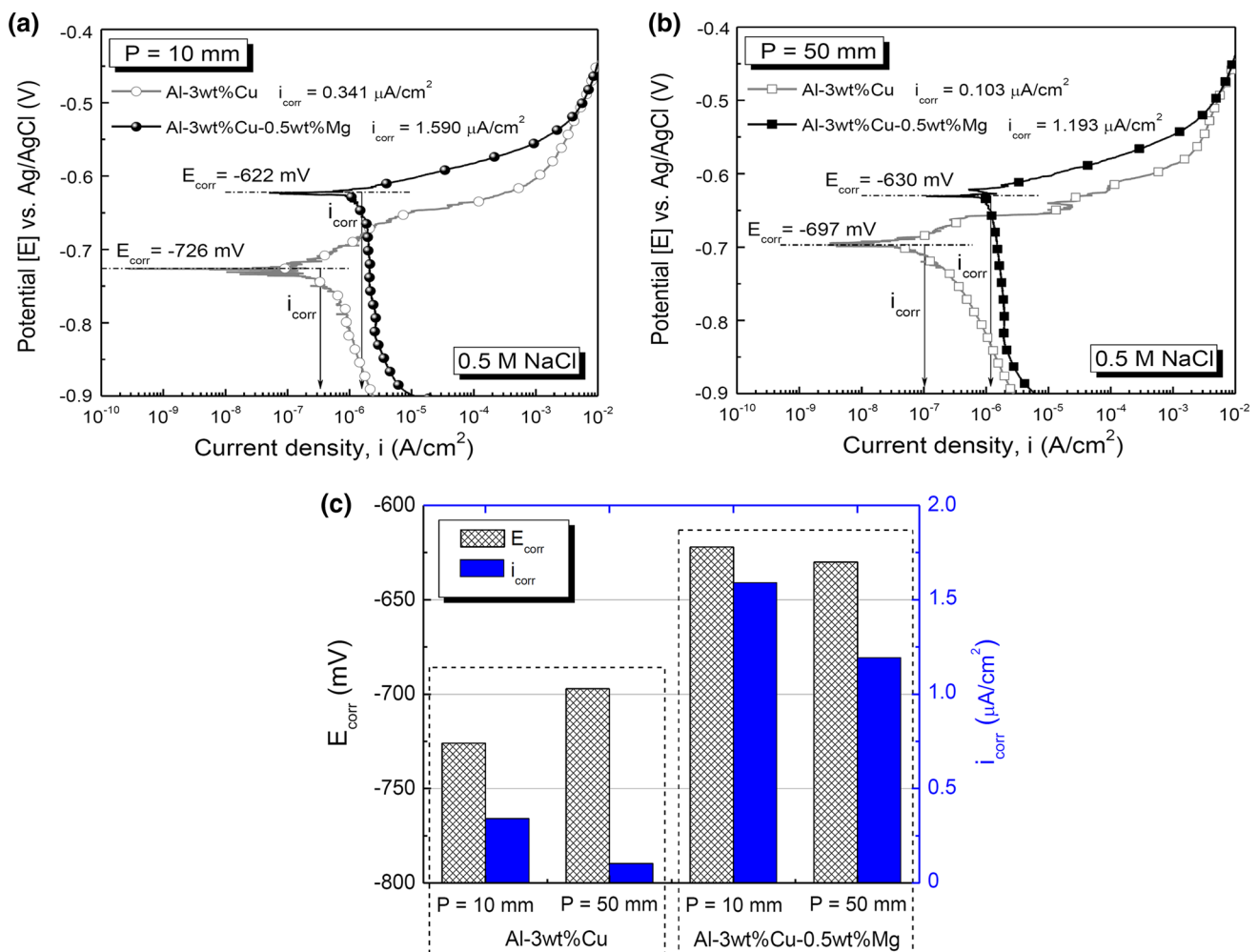
Fig. 11 Experimental potentiodynamic polarization curves of investigated alloys in a 0.5 M NaCl solution at 25 °C for samples extracted from **a** P = 10 mm, **b** P = 50 mm. **c** Corrosion potential (E_{corr}) and corrosion current density (i_{corr}) calculated from potentiodynamic polarization curves

Table 2 Electrochemical parameters of the examined alloys samples in a 0.5 M NaCl solution

Alloy	Sample, P (mm)	E_{corr} (mV)	I_{corr} (μA/cm^2)	R_{pol} (Ω cm^2)	θ_{max} (deg.)
Al–3 wt%Cu	10	− 726	0.341	13,139	80.73
	50	− 697	0.103	16,494	80.33
Al–3 wt%Cu–0.5 wt%Mg	10	− 622	1.590	9147	78.38
	50	− 630	1.193	12,612	77.34

Figure 12 shows typical optical micrographs of both investigated alloys after the corrosion tests in a 0.5 M NaCl solution. Localized corrosion in both the interdendritic zones and the Al-rich (α) matrix can be observed. Similar microstructures have been found by Zossi et al. [31] for Al–5 wt%Cu alloy after corrosion tests in 0.6 M and 1 M NaCl solutions. The authors have observed localized corrosion in both the Al-rich matrix (where the Cu content is 2 wt% or less) and the interdendritic zones (containing higher Cu content). As previously reported [11, 59], the presence of θ-phase particles in the interdendritic regions

induces galvanic interaction between these particles and the adjacent α(Al) matrix that may lead to localized corrosion. Such intermetallics possesses higher corrosion potential as compared to that of the matrix and acts as a cathode in localized corrosion inducing selective dissolution of the surrounding matrix [57]. It is expected that little or no dissolution of these nobler particles occurs.

In order to understand the roles of IMCs of both Al–3 wt%Cu (θ-Al$_2$Cu and Fe-rich intermetallics) and Al–Al–3 wt%Cu–0.5 wt%Mg alloys (θ-Al$_2$Cu, S–Al$_2$CuMg, and Fe-rich particles) on the resulting electrochemical
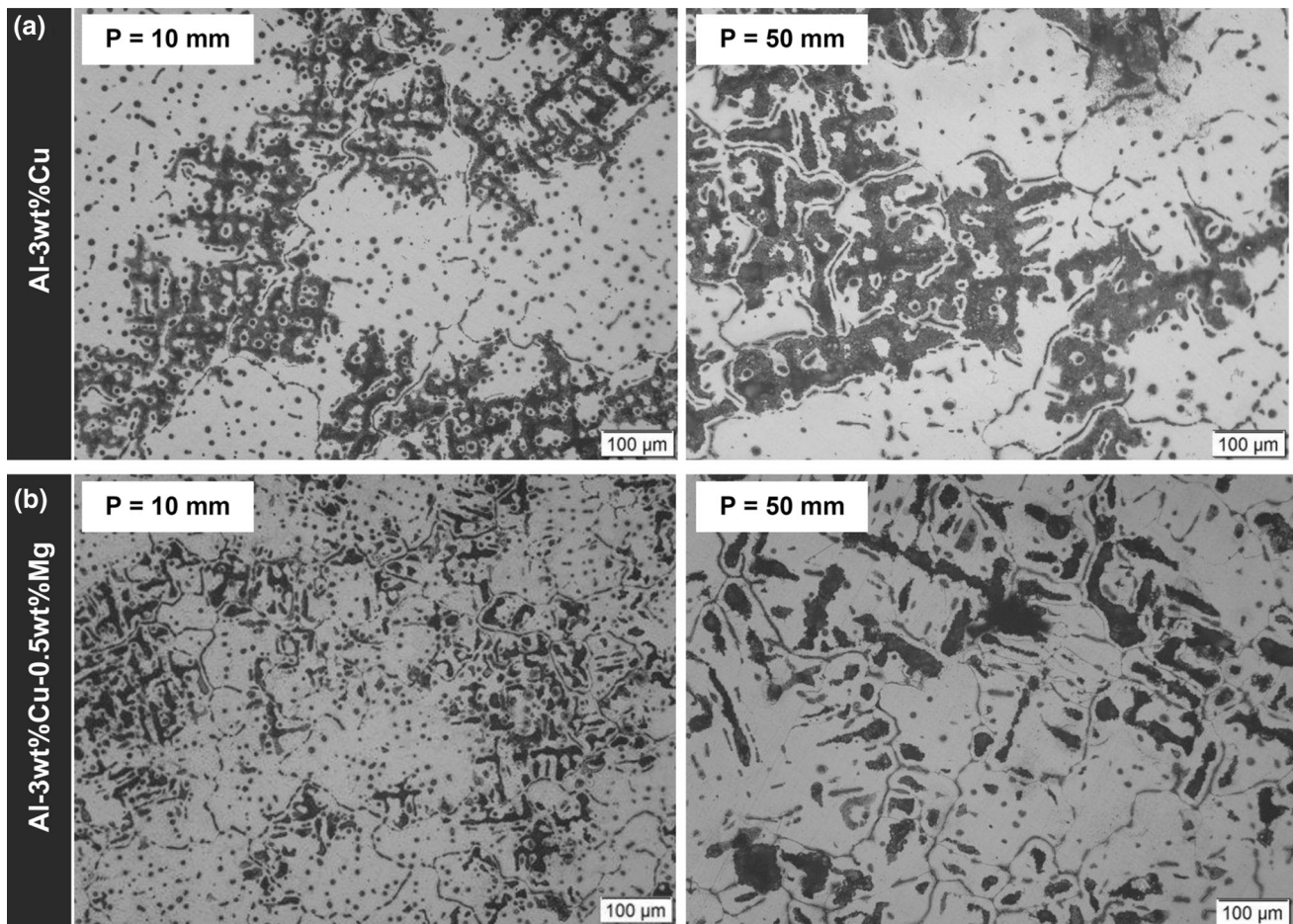
Fig. 12 Optical micrographs of **a** Al–3 wt%Cu, **b** Al–3 wt%Cu–0.5 wt%Mg alloys samples after the corrosion test in 0.5 M NaCl solution at room temperature

corrosion behavior, Fig. 13 shows typical SEM micrographs with EDS elemental mapping of both investigated alloys after the corrosion tests in a 0.5 M NaCl solution. Oxygen concentration in the matrix areas surrounding θ and ω particles for the Al–3 wt%Cu–(0.5 wt%Mg) alloys after the corrosion tests can be seen. Birbilis and Buchheit [11] as well as Li and Dang [59] have also reported that ω-Al_7Cu_2Fe particles sustain relatively large cathodic current densities because of the effect of both Cu and Fe, indicating that it may be an archetypal nobler particle with low dissolution rate and high efficiency for supporting oxygen reduction. Considering the case of the ternary alloy, it has been suggested that the S-Al_2CuMg phase has not dissolved as unique entity. It may be assumed that the S-phase initially dissolves as an anode by the selective dissolution of Mg and Al, leaving a Cu-rich layer with a porous structure (dealloying mechanism). As a probable consequence, the resultant Cu enrichment on the IMC surface may lead this IMC to behave as a local cathode after some unknown time, thus reversing the galvanic relationship between Al_2CuMg and the Al-rich matrix [11, 59].

4 Conclusions

(1) Similar equations may represent the λ_2 evolution with the corresponding solidification thermal variables at the centerline of the longitudinal axis of the horizontally directionally solidified ingot for both Al–3 wt%Cu and Al–3 wt%Cu–0.5 wt%Mg alloys, i.e., the addition of 0.5 wt%Mg to the Al–3 wt%Cu alloy has not affected the experimental growth laws relating λ_2 to G_R and C_R. However, a more complex arrangement of phases in the microstructure of the ternary alloy (α-Al + θ-Al_2Cu + S–Al_2CuMg + Fe-rich particles) has been observed.

(2) The addition of 0.5 wt%Mg to the Al–3 wt%Cu alloy has provided higher HV results, particularly in areas of the horizontally solidified ingot subjected to higher solidification rates. Hall–Petch-type equations have been derived characterizing the experimental variation of HV with λ_2, G_R, and C_R for both investigated alloys. The addition of Mg has contributed to a significant increase in HV.
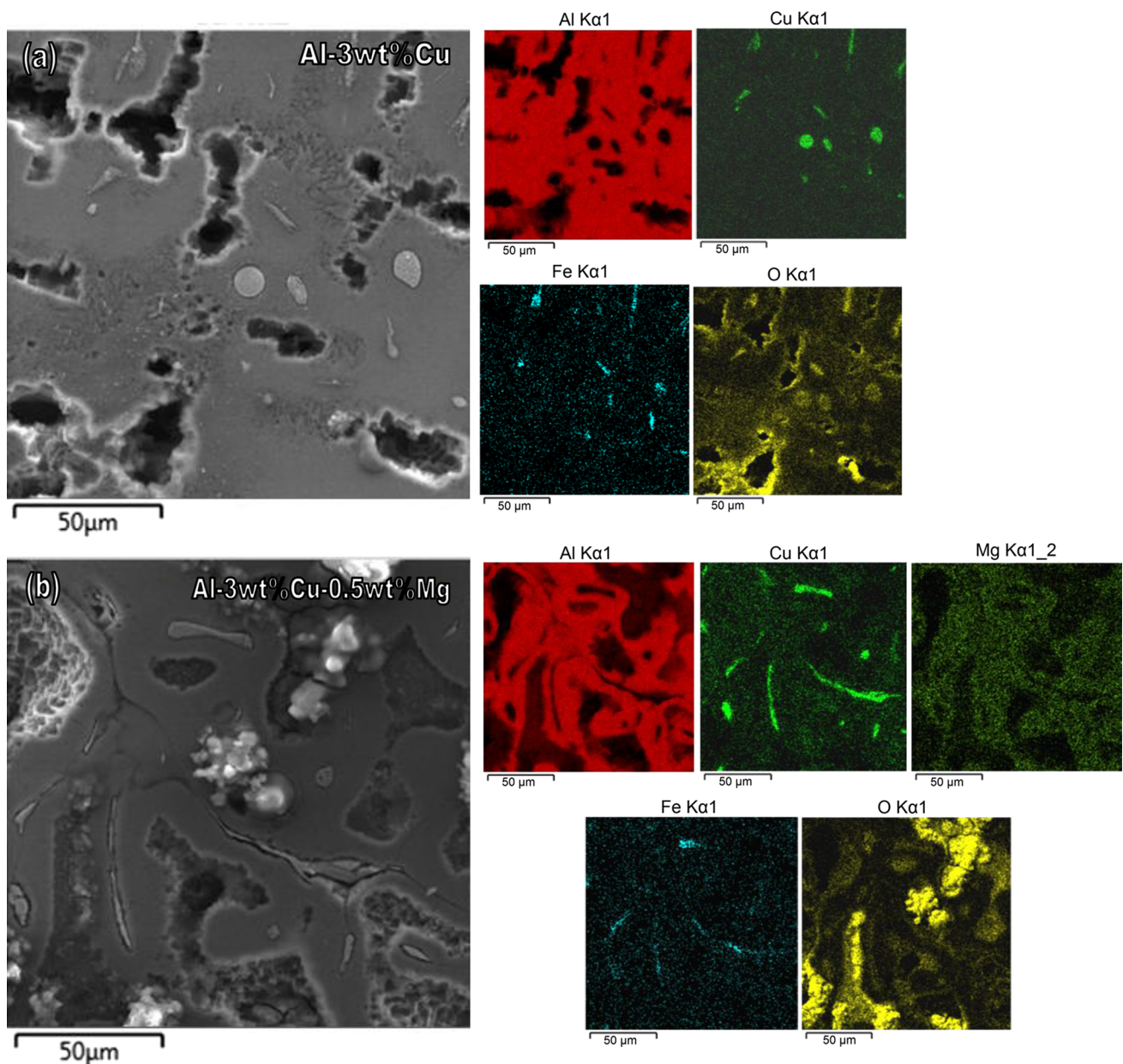
Fig. 13 Typical SEM micrographs with EDS elemental mapping of **a** Al–3 wt%Cu, **b** Al–3 wt%Cu–0.5 wt%Mg alloys after the corrosion test in 0.5 M NaCl solution at room temperature

(3) The polarization curves have confirmed the trend shown by the EIS parameters, indicating that Al–3 wt%Cu–0.5 wt%Mg alloy is comparatively more susceptible to corrosion than the Al–3 wt%Cu alloy. Both alloys have shown localized corrosion in both Al-rich (α) matrix and interdendritic zones. θ and ω particles have acted as cathodes in localized corrosion inducing selective dissolution of the surrounding matrix. S particles may behave as local cathodes after some unknown time due to a dealloying mechanism.

References

[1] R.G. Guan, D. Tie, Acta Metall. Sin. (Engl. Lett.) **30**, 409 (2017)
[2] A. Berkdemir, M. Gündüz, Appl. Phys. A **96**, 873 (2009)
[3] M. Song, Y. He, D. Xiao, B. Huang, Mater. Des. **30**, 857 (2009)

[4] R. Chen, Q.Y. Xu, B.C. Liu, Acta Metall. Sin. (Engl. Lett.) **28**, 173 (2015)

[5] A.S. Barros, I.A. Magno, F.A. Souza, C.A. Mota, A.L. Moreira, M.S. Silva, O.L. Rocha, Met. Mater. Int. **21**, 429 (2015)

[6] G. Sha, R.K.W. Marceau, X. Gao, B.C. Muddle, S.P. Ringer, Acta Mater. **59**, 1659 (2011)

[7] B. Zlaticanin, M. Filipovic, A. Valcic, R. Aleksic, S. Nikolic, B. Radonjic, B. Bosnjak, Mater. Technol. **38**, 25 (2004)

[8] A.M. Al-Obaisi, E.A. El-Danaf, A.E. Ragab, M.S. Soliman, J. Mater. Eng. Perform. **25**, 2432 (2016)

[9] J.M.V. Quaresma, C.A. Santos, A. Garcia, Metall. Mater. Trans. A **31**, 3167 (2000)

[10] B. Zluticanin, S. Duric, B. Jordovic, B. Radonjic, J. Min. Metall. B **39**, 509 (2003)

[11] N. Birbilis, R.G. Buchheit, J. Electrochem. Soc. **152**, B140 (2005)

[12] K. Liu, X. Cao, X.G. Chen, Metall. Mater. Trans. B **43**, 1231 (2012)

[13] B.L. Silva, R.V. Reyes, A. Garcia, J.E. Spinelli, Acta Metall. Sin. (Engl. Lett.) **30**, 528 (2017)

[14] R. Kakitani, R.V. Reyes, A. Garcia, J.E. Spinelli, N. Cheung, J. Alloys Compd. **733**, 59 (2018)

[15] S.N. Yuan, L.N. Jia, L.M. Ma, H. Jiang, H. Zhang, Mater. Sci. Technol. **30**, 75 (2014)

[16] H.M. Jia, X.H. Feng, Y.S. Yang, Acta Metall. Sin. (Engl. Lett.) **30**, 1185 (2017)

[17] X.F. Zhang, J.Z. Zhao, J. Cryst. Growth **391**, 52 (2014)

[18] D. Bouchard, J.S. Kirkaldy, Metall. Mater. Trans. B **28**, 651 (1997)

[19] P.A.D. Jácome, M.T. Fernandes, A. Garcia, A.F. Ferreira, J.A. Castro, I.L. Ferreira, Mater. Sci. Forum **869**, 416 (2016)

[20] E. Acer, E. Çadırlı, H. Erol, H. Kaya, M. Gündüz, Metall. Mater. Trans. A **48**, 5911 (2017)

[21] E. Çadırlı, A. Aker, Y. Kaygisiz, M. Şahin, Mater. Res. **20**, 801 (2017)

[22] L.F. Gomes, B.L. Silva, A. Garcia, J.E. Spinelli, Metall. Mater. Trans. A **48**, 1841 (2017)

[23] O.L. Rocha, L.G. Gomes, D.J. Moutinho, I.L. Ferreira, A. Garcia, Rev. Esc. Minas **68**, 85 (2015)

[24] H.C. de Groh III, M. Yao, Transp Phenom Solidif ASME HTD **284**, 227 (1994)

[25] M.O. El-Bealy, Steel Res. Int. **84**, 565 (2013)

[26] R. Mehrabian, M. Keane, M.C. Flemings, Metall. Mater. Trans. B **1**, 1209 (1970)

[27] T.A. Costa, A.L. Moreira, D.J. Moutinho, M. Dias, I.L. Ferreira, J.E. Spinelli, O.L. Rocha, A. Garcia, Mater. Sci. Technol. **31**, 1103 (2015)

[28] M. Dias Filho, R.H. Kikuchi, T.A. Costa, A.L. Moreira, O.L. Rocha, Matéria **20**, 47 (2015)

[29] A.J. Vasconcelos, R.H. Kikuchi, A.S. Barros, T.A. Costa, M. Dias, A.L. Moreira, A.P. Silva, O.L. Rocha, An. Acad. Bras. Ciênc. **88**, 1099 (2016)

[30] Y. Kaygisiz, N. Maraşli, Phys. Met. Metallogr. **118**, 389 (2017)

[31] A.M. Zossi, A. Morales Torres, S.M. de De Micheli, H. Biloni, Metall. Trans. A **7**, 1489 (1976)

[32] W.R. Osório, C. Siqueira, C.A. Santos, A. Garcia, Int. J. Electrochem. Sci. **6**, 6275 (2011)

[33] B.B. Yu, H. Yan, J.B. Zhu, J.L. Liu, H.G. Li, Q. Nie, Acta Metall. Sin. (Engl. Lett.) (2018). https://doi.org/10.1007/s40195-018-0782-9

[34] W.R. Osório, D.M. Rosa, A. Garcia, Mater. Des. **34**, 660 (2012)

[35] W.R. Osório, L.C. Peixoto, D.J. Moutinho, L.G. Gomes, I.L. Ferreira, A. Garcia, Mater. Des. **32**, 3832 (2011)

[36] D.L. Soares, A.S. Barros, M. Dias, A.L. Moreira, J.C. Filho, A.P. Silva, O.L. Rocha, Int. J. Electrochem. Sci. **12**, 413 (2017)

[37] J. Esquivel, R.K. Gupta, Acta Metall. Sin. (Engl. Lett.) **30**, 333 (2017)

[38] O.L. Rocha, C.A. Siqueira, A. Garcia, Metall. Mater. Trans. A **34**, 995 (2003)

[39] G. Garmong, C.G. Rhodes, Metall. Mater. Trans. B **3**, 533 (1972)

[40] C.G. Rhodes, G. Garmong, Metall. Mater. Trans. B **3**, 1861 (1972)

[41] W.R. Osório, J.E. Spinelli, A.P. Boeira, C.M. Freire, A. Garcia, Microsc. Res. Techniq. **70**, 928 (2007)

[42] E.C. Araújo, A.S. Barros, R.H. Kikuchi, A.P. Silva, F.A. Gonçalves, A.L. Moreira, O.L. Rocha, Metall. Mater. Trans. A **48**, 1163 (2017)

[43] E. Acer, E. Çadırlı, H. Erol, M. Gündüz, Metall. Mater. Trans. A **47**, 3040 (2016)

[44] M. Günduz, E. Çadırlı, Mater. Sci. Eng., A **327**, 167 (2002)

[45] K. Murakami, T. Fujiyama, A. Koike, T. Okamoto, Acta Metall. **31**, 1425 (1983)

[46] M. Costa, F. Souza, I. Magno, C. Loyaza, J. Nascimento, A. Barros, O. Rocha, Mater. Sci. Medzg. **23**, 124 (2017)

[47] C.H.U. Gomes, R.H.L. Kikuchi, A.S. Barros, J.N.S. Silva, M.A.P.S. Silva, A.L.S. Moreira, O.F.L. Rocha, Mater. Res. **18**, 1362 (2015)

[48] L.G. Gomes, D.J. Moutinho, I.L. Ferreira, O.L. Rocha, A. Garcia, Appl. Mech. Mater. **719–720**, 102 (2015)

[49] J.D. Faria, C. Brito, T.A.P.S. Costa, N.C. Verissimo, W.L.R. Santos, J.M.S. Dias Filho, A. Garcia, N. Cheung, Matéria **20**, 992 (2015)

[50] M. Peres, C. Siqueira, A. Garcia, J. Alloys Compd. **381**, 168 (2004)

[51] M.V. Canté, J.E. Spinelli, I.L. Ferreira, N. Cheung, A. Garcia, Metall. Mater. Trans. A **39**, 1712 (2008)

[52] C. Brito, T.A. Costa, T.A. Vida, F. Bertelli, N. Cheung, J.E. Spinelli, A. Garcia, Metall. Mater. Trans. A **46**, 3342 (2015)

[53] C. Brito, F. Bertelli, M.A.P. Castanho, P.R. Goulart, N. Cheung, J.E. Spinelli, A. Garcia, Sci. Technol. Mater. **29**, e65 (2017)

[54] J. Spinelli, D. Rosa, I. Ferreira, A. Garcia, Mater. Sci. Eng., A **383**, 271 (2004)

[55] D. Carvalho, J. Rodrigues, D. Soares, J. Aviz, A. Barros, M. Silva, O. Rocha, I. Ferreira, A. Moreira, Mater. Sci. Medzg. **24**, 18 (2018)

[56] F.Y. Xie, T. Kraft, Y. Zuo, C.H. Moon, Y.A. Chang, Acta Mater. **47**, 489 (1999)

[57] Z. Szklarska-Smialowska, Corros. Sci. **41**, 1743 (1999)

[58] D. Song, A.B. Ma, J.H. Jiang, P.H. Lin, L.Y. Zhang, Prog. Nat. Sci.: Mater. Int. **21**, 307 (2011)

[59] J. Li, J. Dang, Metal **7**, 84 (2017)